DESIGN OF A WALL-LESS PROPORTIONAL COUNTER FOR MICRODOSIMETRY IN NANOMETER DIMENSIONS

A Thesis

by

SRIPRIYA RAYADURGAM

Submitted to the Office of Graduate Studies of
Texas A&M University
in partial fulfillment of the requirements for the degree of

MASTER OF SCIENCE

May 2005

Major Subject: Health Physics

DESIGN OF A WALL-LESS PROPORTIONAL COUNTER FOR MICRODOSIMETRY IN NANOMETER DIMENSIONS

A Thesis

by

SRIPRIYA RAYADURGAM

Submitted to Texas A&M University
in partial fulfillment of the requirements
for the degree of

MASTER OF SCIENCE

Approved as to style and content by:

Leslie A. Braby (Chair of Committee)	John R. Ford (Member)
Warren D. Reece (Member)	Nancy D. Turner (Member)

William E. Burchill
(Head of Department)

May 2005

Major Subject: Health Physics

ABSTRACT

Design of a Wall-less Proportional Counter for

Microdosimetry in Nanometer Dimensions. (May 2005)

Sripriya Rayadurgam, B.Sc., University of Madras;

M.Sc., University of Madras

Chair of Advisory Committee: Dr. Leslie A. Braby

Knowledge of energy deposition in biological cells at nanometer dimensions is essential to understand the biological effects of radiation. This work has resulted in the development of a practical tool to study such energy deposition experimentally, at nanometer dimensions.

The main contribution of this research is the design of a cylindrical wall-less proportional counter of 1mm height by 1mm diameter. A wall-less detector (also called grid-walled detector) overcomes the so-called "wall effect", an experimental artifact that introduces distortions in the radiation energy measurements. An important feature of this detector that distinguishes it from other detectors is its modular design. This allows the detector to be repaired or modified, when necessary, without having to completely disassemble it. Novel design techniques were adopted resulting in a functional detector that can simulate cellular sites as small as 10 nanometers, approximately the size of many molecules in the cell.

The detector was tested with a 1 microcurie sealed Am-241 source, which primarily emits monoenergetic alpha particles of energy 5.57 MeV. Microdosimetric spectra

analysis for alpha particles and its delta rays from Am-241 were performed for simulated site sizes ranging from 500nm to 10nm. Initial studies to validate the detector design have confirmed good detector performance. We believe this work will serve as a vital platform for bridging the experimentally measured energy spectra to the biological effects of alpha and delta radiations.

ACKNOWLEDGMENTS

I would like to thank Dr. Leslie A. Braby, my advisor, for his guidance and support. His time and effort are greatly appreciated.

Many thanks to my parents, my brothers and my sisters for being a source of strength all through this work.

I would like to thank Tony Restivo who taught me the nuances of machine shop and Dr.Wen Hsing Hsu for helping me out with the photography.

TABLE OF CONTENTS

Page

CHAPTER Page

LIST OF FIGURES

FIGURE Page

LIST OF TABLES

CHAPTER I

INTRODUCTION

When humans are exposed to ionizing radiations, the risks that limit occupational exposure are tumor formation and germ-cell mutations. These risks are thought to be the result of molecular lesions produced by radiation. The lesions are induced by energy deposited in the form of highly structured tracks of atomic ionization and excitation along the paths of the primary and secondary charged particles. The ionization pattern in the track has a direct impact on the cellular mechanisms and so there is a very great need to understand the microscopic structure of the individual tracks and hence the energy deposition at the cellular and the subcellular level (1). The study of energy deposition in cellular and subcellular targets, i.e., in sites of micrometer and nanometer dimensions, is termed Microdosimetry.

Microdosimetry, a relatively new concept in the field of radiation physics, began in the 1950's when Dr. Harold H. Rossi attempted to measure Linear Energy Transfer (LET), the statistical average of energy loss per unit path length, for various radiation fields. He discovered that LET is a poor representation of energy distribution at the cellular level and started to build refined instruments, spherical tissue equivalent proportional counters, to study the probability of local energy densities in microvolumes. He developed the concepts of measuring energy deposition due to radiation insult at the cellular level, which would determine the effects of radiation (2). This is now called

---

This thesis follows the style and format of *Radiation Research.*

Regional Microdosimetry, and includes an experimental procedure to measure energy deposition in small sites without regard to the microscopic distribution of ionization within the site.

Dr. A. M. Kellerer picked up the study and developed the concept of structural microdosimetry, which involves the study of microscopic distribution of energy deposition without reference to a bounded volume. This study involves the analysis of highly structured tracks of ionization and excitation along the paths of primary and secondary radiations. The analysis of track structure is not limited to the location of energy deposition events but also includes the history of the ionizing radiation prior to its interaction at the site in question and the migration of energy between two sites (3).

Since it is not possible to directly measure the patterns of radiation tracks at this microscopic level, theoretical and experimental studies are used in a complementary way to get a better understanding of the energy deposition process.

Theoretical studies are performed by Monte Carlo track structure simulation, where a large number of tracks of a given type are simulated and randomly superimposed onto a geometric volume of interest. This simulation takes into consideration all the probable interactions of the incident charged particle with the volume and the calculation for the particle is allowed to proceed until either a preset number of interactions occurs, or a given ion track length is generated. The data obtained from these simulations are used as inputs in specialized algorithms to compute the microdosimetric quantities for biological application. To cross check the results obtained from theoretical studies, experimental studies are performed. The need for theoretical and experimental studies is mutual as both the methods have their own limitations (4).

Experimental microdosimetry usually refers to the measurement of energy deposition in sites with small dimensions, usually using low pressure tissue-equivalent proportional counters, even though several alternate detectors have been developed. Proportional counters used in microdosimetric studies are gas-filled detectors, typically spherical or cylindrical, with approximately the same atomic composition as that of the solid cellular and subcellular structures. In these gas-filled cavities, which simulate the biological structures, the energy absorption process takes place over a significantly larger distance than in solids. This magnification negates the need to measure energy deposition processes in micrometer-sized detectors. By collecting the charges due to ionization in the low density gas and processing with the appropriate electronics, the microdosimetric quantities of interest are measured.

With advancements being made in theoretical and experimental studies, microdosimetry has found its applications in many areas other than radiobiology.

In radiotherapy, where knowledge about LET for different therapeutic radiations is required to study the oxygen effect in tumor treatment or to study the LET dependent relative biological effect (RBE), microdosimetry is the obvious choice to document the differences of radiation quality.

In radiation protection, measurement of the probability density of lineal energy is a major, if not the only, method employed to study the dose equivalent for very high energy radiations.

In the field of microelectronics, where knowledge about single event radiation interactions becomes crucial, microdosimetry has a pivotal role. A single charged particle

interacting with a micro-capacitor could impart enough energy to alter the voltage across the capacitor resulting in the change of a critical binary state of the system.

Microdosimetry also plays a vital role in dosimetry studies on manned space flight, where most of the dose is due to individual high energy events which are widely separated in time.

This research focuses on the design of a wall-less cylindrical proportional counter, 1mm in diameter by 1mm in length, for the study of microdosimetric spectra of α particles and their δ rays at nanometer dimensions. Though solid wall detectors as small as 1mm diameter have been built, the proposed detector is the first modular grid walled (wall-less) detector built to measure the microdosimetric spectra of charged particles and their δ rays, in simulated volumes as small as a few nanometers.

The objective of a wall-less detector is to obtain a microdosimetric spectrum devoid of the distortion caused by the solid wall in a detector. The type of wall effect that creates concern in case of a heavy charged particle, like α particles, is the δ ray effect. When a charged particle interacts with the tissue equivalent medium δ rays may be produced. These δ rays dissipate their kinetic energy along a separate track from that of the primary charged particle. An artifact in experimental microdosimetry is the so called wall effect. It occurs when the primary charged particle and one or more of its δ rays that were produced in the wall (and would have missed the detector volume if the density was constant) appear simultaneously in the gas cavity. In such cases we have no way to distinguish between the energy deposited by the α particles and by the δ rays. A wall-less counter eliminates this artifact.

The structure of the individual tracks in terms of energy deposition in nanometer tissue equivalent volumes is important because of the clustering of ionizations that may lead to multiply damaged sites in cellular DNA. Multiply damaged sites have enhanced biological significance and studies have shown that dense ionization tracks from high LET radiations, like α particles, produce Multiply Damaged Sites (5). Many of these sites result from the superposition of the primary track and a δ ray track.

The recent growing concern about biological processes initiated by δ rays from charged particle interactions and the need to know more about α particles, a major contributor in the background radiations, have prompted this study. It is interesting that radon and its decay products, primarily α emitters, contribute 55% of the background effective dose, averaged over the United States. Radon is common in indoor air and uranium miners who were exposed to high levels of radon daughters have developed lung cancers.

When talking about the interactions of radiations at the microdosimetric level, our quantitative description of interactions shifts from conventional average quantities, like absorbed dose and LET, to specific energy and lineal energy. These microdosimetric quantities and the standard representation of microdosimetric spectrum are described in Chapter II. It is followed by the theory on microdosimetric detectors in Chapter III and the procedures behind the designing of the detector in Chapter IV. The results obtained are documented in Chapter V followed by conclusions from the results in Chapter VI.

CHAPTER II

MICRODOSIMETRIC QUANTITIES

The traditional way to quantitatively describe the interaction of an ionizing radiation field with the absorbing medium is by defining the absorbed dose, *D*, which is the limit of the ratio of the energy absorbed within a small volume element by the mass of the medium in that element as the mass approaches zero. When we are dealing with the interaction of ionizing radiations at volumes of the order of micrometer dimensions, absorbed dose, an average quantity, is not the ideal quantity to describe the energy deposition process. This is because at smaller target sizes the stochastic nature of radiation interactions become increasingly important and the energy deposition may have any value depending upon whether the particle track completely misses the site, or partially passes through the site, or the entire track gets absorbed in the site of interest. To describe the energy deposition process at microdosimetric level, the stochastic quantity, specific energy is used. Figure 1 schematically explains the concept of specific energy (6).

Left side of Figure1 represents the interaction of different charged particles, from neutron irradiation. Different line lengths represent charged particles of different energy and the different line thicknesses the different rates of energy loss. The series of circles represents sites of few micrometers diameter. Assuming that this figure represents the time integral of the energy deposition process then the absorbed dose in each site has a

different value depending upon the number of charged particles and the type of particle that have interacted with the site. Taking an average of these values and representing it as the average energy absorbed per unit mass would grossly under or over estimate the energy deposition in each site. For this reason the energy deposited per unit mass in each site is referred to as the specific energy and absorbed dose is used for the average of the specific energy over all the sites.

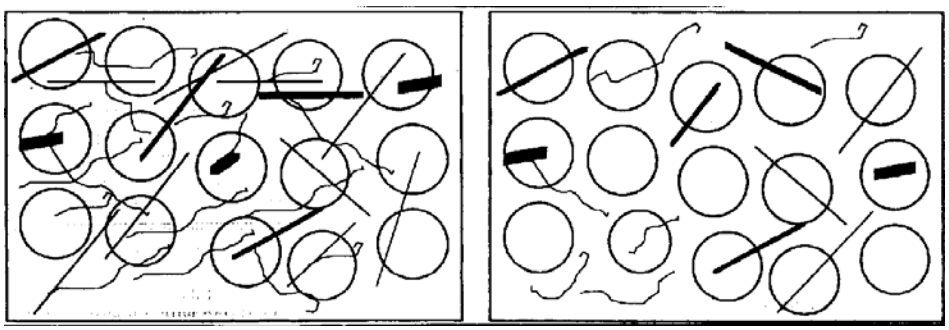

FIGURE 1: Schematic Representation of Specific Energy.
(Left Side) Schematic representation of a neutron radiation field interacting with a medium. (Right Side) Schematic representation of a radiation field that would result in an average of one energy deposition event in any one site (3).

The right side of Figure 1 represents a situation where at most one charged particle interacts with the site. In such cases the specific energy deposited in each site arises from the intersection of a single charged particle track called an event.

As microdosimetry does not deal with the average energy absorbed per unit mass of tissue, but with the nature of the energy deposition by single or relatively few interactions, the energy transfer events are governed by Poisson statistics which give predictions of the magnitude and characterizations of effects produced.

Specific Energy

The energy deposited in a defined site by a particle, together with all of the secondary electrons produced by it, is called the energy imparted, ε. The mean specific energy, z, is the total energy imparted by all events, ($\Sigma\varepsilon$), per unit mass of microdosimetric volume, usually expressed in terms of Gy.

$$z = \frac{(\sum \varepsilon)}{m} \tag{1}$$

Unlike the average quantity, absorbed dose, the specific energy is a stochastic quantity and cannot be expressed in terms of a point function, in differential form. So the probability distribution of z is considered. The probability that the specific energy, produced in multiple events by protracted irradiation, is between [z, $z+dz$] is given by $f(z)dz$. Since the value of z may also be zero, if the volume size is decreased, any statements of z and $f(z)$ must contain information on the size of the volume (3).

When z is averaged over a large number of individual targets, such as cells in tissue, (as shown in the left side of Figure 1) all values of z may occur. The average value of z over all the locations becomes equal to the average dose, D. This implies that the mean value, $\bar{z}$, of the probability distribution $f(z)$ is equal to absorbed dose, D.

Also, if the specific energy deposited in each site arises from the interaction of only a single charged particle track, (as shown in the right side of Figure 1) the probability distribution of z is represented by $f_1(z)$ and $f_1(z)$ is not defined at $z = 0$.

Lineal Energy

In many areas of radiation science, a correlation has been found between the level of biological effect and some measure of the ionization density along the tracks of the ionizing secondary particles. Of the various quantities that have been defined over the years, Linear Energy Transfer (LET) has been accepted as the principal quantity. The microdosimetric analogue of LET is lineal energy which is defined as the quotient of energy imparted in a single event, ε, divided by the mean chord length, $\bar{l}$, of the volume traversed by charged particles,

$$y = \frac{\varepsilon}{\bar{l}} \tag{2}$$

y refers only to the energy imparted in a single event and is usually expressed in terms of keV/μm. Thus, lineal energy is not restricted by an energy limitation like the non-stochastic concept, the restricted LET, but by a geometric cut off based on the size of the volume under consideration. Like *z, y* is also subject to a probability distribution *f(y)*. For any convex body having surface area *S* and volume *V* traversed by isotropic chords, the mean chord length, $\bar{l}$, maybe found by Cauchy's Theorem (3):

$$\bar{l} = 4\frac{V}{S} \tag{3}$$

The relation for a right circular cylinder becomes:

$$\bar{l} = \frac{2dh}{(d+2h)} \tag{4}$$

In the case of a cylindrical detector with equal height and diameter, the average chord length is the same as that for a sphere:

$$\bar{l} = \frac{2}{3} d \tag{5}$$

The single event z distribution, $f_1(z)$, and $f(y)$ are dependent on the simulated site size by the following relation (3):

$$z = \frac{4y}{\rho s} \tag{6}$$

In most applications of microdosimetry the density is usually taken as that of tissue, $1 g/cm^3$ .The specific energy z is expressed in the unit Gray, y in keV/μm and d in μm. Substituting the surface area of a cylinder for equal height and diameter $(S = 2\pi r(h+r))$, the relation becomes:

$$z = \frac{0.136y}{(2r)^2} Gy \tag{7}$$

Microdosimetric Spectral Analysis

As we obtain the spectrum from proportional counter, the pulse height distribution observed by measurement is proportional to y and z_1. The shape of the distribution is dictated by the stochastic nature of energy deposition events. When this is the case, the recorded spectrum is determined by a number of random factors and hence governed by Poisson statistics. Kellerer has provided a thorough analysis of the random factors that determine the shape of the pulse height distribution (7).

The total variance V_T is due to six processes that are subject to statistical fluctuations and hence characterized by probability density distributions (3). They are:

1. The distribution of the number of energy deposition events.
2. The LET distribution of the particles.
3. The distribution of the path lengths of particles in the site.
4. The distribution of the number of collisions.
5. The distribution of energy imparted in individual collisions.
6. The distribution of the fraction of this energy retained in the site.

The analysis of spectra is based on the sum of the variances of these individual processes. The relative variance, V, of a measured spectrum is obtained by determining the first and the second moments of the distribution, and is given by:

$$V = \frac{\sigma^2}{m_1^2} = \left(\frac{m_2}{m_1^2} \right) - 1 \tag{8}$$

Where: m_1 is the first moment of a distribution $f(x)$ and
m_2 is the second moment of a distribution $f(x)$.

The first moment, m_1, is the expectation value, and is given by

$$m_1 = \int x f(x) dx \tag{9}$$

The second moment, m_2, is thus

$$m_2 = \int x^2 f(x) dx \tag{10}$$

For the microscopic distributions $f(y)$ and $f(z)$, the first moments of the spectra are called the frequency averages and are given by

$$y_F = \int y f(y) dy \qquad \text{and} \qquad z_F = \int z f(z) dz \tag{11}$$

The dose averages, y_D and z_D are the ratios of the second to the first moments:

$$y_D = \frac{1}{y_F}\int y^2 f(y)dy \qquad \text{and} \qquad z_D = \frac{1}{z_F}\int z^2 f(z)dz \tag{12}$$

Thus the relative variances of y and z reduces to:

$$V_y = \frac{y_D}{y_F} - 1 \qquad \text{and} \qquad V_z = \frac{z_D}{z_F} - 1 \tag{13}$$

Representation of Microdosimetric Spectra

Microdosimetric event-size spectra are almost always presented as lineal energy spectra because the spatial relationship between ionizations along the tracks of the charged particles is crucial to our understanding of the biological effects of radiation. A further advantage of lineal energy representation of event size spectra is that it provides a means of evaluating quality factors and the dose equivalent directly from the microdosimetric measurements.

In case of lineal energy distribution $f(y)$, which involves single events, the variance due to the number of energy deposition events is zero. The contribution of LET variation becomes a concern only when the simulated site size is greater than 500 nm. In this work, as we are dealing with monoenergetic α particles and site size simulation well below 500 nm, the LET variance factor can be neglected. Studies have shown that for α particles, the relative variance of triangular path length distribution dominates the spectrum. The other factor that changes the spectrum is energy loss straggling. These are depicted in Figure 2.

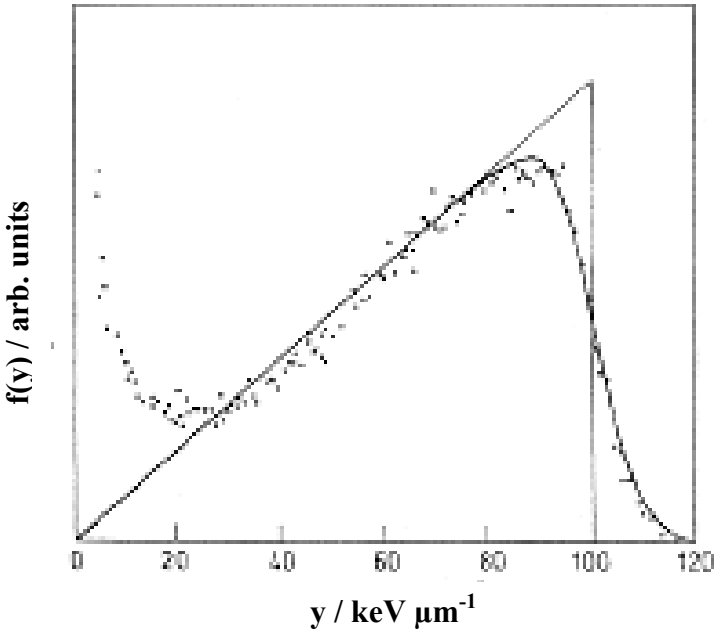

FIGURE 2: Lineal Energy Spectra of α Particles.
Solid Line: Theoretical chord length distribution in a sphere. Curve: Lineal energy spectrum from a wall-less counter in a 1μm diameter site, when exposed to 5.3-MeVα particles (3).

Thus the lineal energy spectrum of α particles will have fluctuations due to path length distributions, energy loss straggling and δ rays.

CHAPTER III

THEORY

Proportional Counter Theory

The fundamental principle behind any radiation detector is to detect and, in most cases, measure the changes produced by the interaction of radiation with the detector medium. In a proportional counter, gas is used as a medium of interaction and the ionizations produced as a result of interactions are measured, providing information about the energy deposited. Thus, the output pulses in a proportional counter are distinguished by their energy. Proportional counters are operated in pulse mode, which enables us to measure the energy deposited per ionizing event.

The unique characteristic of a proportional counter is its ability to amplify the ionization produced by a single particle event into a signal that is large enough to be distinguished from electronic noise and thereby be detected (8, 9). This phenomenon, called gas multiplication, is the result of an electron avalanche, a process in which a relatively small number of ions produced by a single charged particle track are multiplied through secondary ionizations due to the high electric field, near the surface of a small diameter anode. Gas multiplication depends on several factors, but in general, depends on increasing the electric field within the detector to a high value so that electrons gain sufficient energy between collisions with gas molecules as they drift toward the anode that they create secondary ionizations in those collisions (8, 9). Under proper conditions

the number of electrons in the avalanche can be kept proportional to the number of primary electrons.

Experimental studies in microdosimetry employ proportional counters to relate the energy deposited in the gas medium of the detector to that in the radiation sensitive targets in mammalian cells, DNA, for example.

Tissue Equivalence

Tissue equivalence in a proportional counter is obtained by using gases which have the same atomic composition as tissue. Since radiation interacting with two different materials of the same atomic composition but different chemical combinations would result in the same energy deposition, a multitude of choices for tissue equivalent gases are available. From the mixtures of the four most common elements, hydrogen, carbon, oxygen and nitrogen, materials with energy absorbing properties equivalent to tissue can be obtained. The two most common tissue equivalent gases in use are methane and propane based obtained by mixing carbon dioxide and nitrogen with methane or propane. Pure propane, the gas used in this experiment, has better counting characteristics in terms of gas gain and is nearly tissue equivalent (6).

Size Equivalence

It is a very well proven fact that the radiation sensitive targets in mammalian cells are contained in the cellular nucleus and the cellular effects are initiated by damage to DNA.

Many authors suggest that the relevant biological entities have dimensions in the range of nanometers (1,3). In order to relate the energy deposition to cellular and sub-cellular objects, the microdosimetric detectors are operated to simulate site sizes in the micro and nanometer range. To achieve this size scaling, the physical size of the detector and the density of the gas are used as variables, as they form a conjugate pair in controlling the site size simulation (9).

The physical area of the detector is directly proportional to the counting rate and the size of the detector is chosen according to its application. In the case of a low dose rate radiation, a larger diameter detector is used in order to obtain adequate counting statistics in a reasonable time and in case of a high dose rate radiation, a smaller size is chosen to avoid pulse pile up and higher dead time. But to simulate site sizes in the nanometer range, the diameter of the detector should be small. This was realized when efforts by researchers to operate a 25mm diameter detector to simulate 0.1 micrometer site size were impaired by poor energy resolution due to the gas avalanche diameter approaching the detector diameter. Dr. P. J. Kliauga (10) was the first to recognize that if the dimensions of the detector were reduced, it would be possible to simulate site sizes in the nanometer range. That leaves a single variable, the pressure of the gas, which controls the site size simulated by the detector.

The energy deposited in a site, by a charged particle, is the product of the mass stopping power, the density of the medium and the path-length of the ionizing radiation across the volume, or (6):

$$E = \frac{dE}{\rho dX}\rho\Delta X \tag{14}$$

where E is the local energy deposition;

$\frac{dE}{\rho dX}$ is the mass stopping power of the target material;

ρ is the density of the target medium;

ΔX is the path-length across the target volume.

The energy deposition in the tissue *(E_t)* should be equal to the energy deposition in the gas material of the detector *(E_g)*, for the simulation to hold. Then

$$E_g = E_t \tag{15}$$

i.e., $$E_g = (dE/\rho dX)_g \rho_g \Delta X_g = E_t = (dE/\rho dX)_t \rho_t \Delta X_t \tag{16}$$

By definition of tissue equivalence, the mass stopping power of tissue and tissue equivalent gas are the same. So Equation 16 becomes:

$$\rho_g \Delta X_g = \rho_t \Delta X_t \tag{17}$$

Equation 17 gives the condition, the product of the gas density and the gas cavity diameter should be equal to the product of the tissue volume diameter and tissue density, to achieve microscopic tissue volume simulation.

The density of the tissue, the size of the tissue volume, and the size of the detector volume are known. The gas density which controls the site size simulation, can be obtained from Equation 17,

$$\rho_g = \rho_t \frac{\Delta X_t}{\Delta X_g} \tag{18}$$

Thus by minimizing the detector volume, higher gas density is obtained, for a given simulated site size, resulting in better pulse height resolution (see section on gas

multiplication). Higher gas density increases the probability of interaction, which in turn increases the performance of the detector.

If the fill gas is not tissue equivalent, the gas density required to simulate site sizes are obtained by substituting the appropriate values of stopping power in Equations 16 and 17.

Substituting $\rho_t = 1.04 g/cm^3$, the density of muscle tissue (11,12) and $\Delta X_g = 1 mm$, the size of the detector used in this experiment, in Equation 18, the gas density for different site sizes is calculated. By using the gas density values in ideal gas equation, the gas pressure required to simulate different site sizes can be obtained.

Ideal gas law equation

$$PV = nRT \tag{19}$$

can also be written as

$$P = \frac{\rho}{M} RT \tag{20}$$

where ρ is the density of propane in gm/cm^3;

$M = 44.096 g$, molecular weight of propane (13, 14);

$R = 62.365 \times 10E3 \frac{cm^3 - torr}{mole - K^\circ}$;

$T = 293 K^\circ$, $RoomTemperature$.

From Equation 20, the pressure required to simulate different site sizes are calculated and shown in Table 1 along with the corresponding gas density values.

The efficiency of proportional counters to simulate tissue equivalent nanometer site sizes is increased with its inherent ability to produce good gas gain characteristics.

TABLE 1: Operational Gas (Propane) Pressure and Density Values for Different Simulated Site Sizes

Simulated Site Size	Required Operational Pressure in Torr	Gas Density (g/cm^3)
1µm	430.9	1.04E-03
500nm	215.4	5.20E-04
300nm	129.3	3.12E-04
200nm	86.2	2.08E-04
100nm	43.1	1.04E-04
50nm	21.5	5.20E-05
20nm	8.61	2.08E-05
10nm	4.31	1.04E-05

Gas Multiplication Factor

In a cylindrical proportional counter, the electric field E depends on the anode radius a, the cathode radius b, the anode voltage V and the radial distance r, as (9)

$$E = \frac{V}{r \ln\left(\frac{b}{a}\right)} \tag{21}$$

Equation 21 implies that the maximum value of the electric field would appear in the immediate vicinity of the anode wire where r is small. By reducing the thickness of the wire *(a)*, smaller values of r can be used, resulting in a larger electric field.

The fractional increase in the number of electrons per unit path length during gas multiplication assumes an exponential growth and is given by

$$G = \frac{N}{N_0} = e^{\alpha d} \tag{22}$$

where G represents the gain;
N represents the number of electrons resulting from multiplication;
N_0 represents the initial number of electrons;
d represents the distance over which the electrons are accelerated; and
α is termed as the first Townsend coefficient.

Using a first approximation the first Townsend coefficient *(α)* given by

$$\frac{\alpha}{p} = Ae^{-Bp/E} \tag{23}$$

where p is the gas pressure usually measured in torr;
E is the electric field in Vcm^{-1};
A is a constant and is the mean number of collisions per cm; and
B a constant, is a quotient of the mean ionization potential of the gas, I, and the mean free path for ionizations.

An empirical expression for gas multiplication factor in terms of the detector parameters and applied voltage was derived by Diethorn (8). The assumptions underlying this derivation are that the multiplication process is only through electron collisions and the space charge effects are negligible. Taking into consideration the radial dependence of the Townsend coefficient for a cylindrical geometry, the gas multiplication factor is given by

$$\ln M = \frac{V}{\ln\left(b/a\right)} \bullet \frac{\ln 2}{\Delta V} \bullet \left(\ln \frac{V}{pa \ln\left(b/a\right)} - \ln K \right) \tag{24}$$

where M is the gas multiplication factor;
V is the applied voltage;
ΔV is the potential difference through which an electron moves between successive ionizing events;
a is the anode radius;
b is the cathode radius;
p is the gas pressure;
K represents the minimum value of E/p below which the multiplication cannot

occur.

Diethorn's approach treats both the constants ΔV and K as empirically fitted parameters. This procedure is sufficient to model experimental data over limited ranges of pressure, voltage and counter dimensions. To describe the operation of detector at micro and nanometer site sizes, a third parameter has to be introduced to describe electron avalanches at low pressures.

In order to obtain uniform multiplication for all the ion pairs formed by the original ionizing event, the gas multiplication region must be confined to a very small volume around the anode as compared to the volume of the detector. Under this condition, all the original ion pairs are formed well outside the avalanche region and undergo the same multiplication process irrespective of the location of the original event. This enables the counter to have a very good energy resolution where there is no variance in the number of ion pairs other than the normal ionization statistics.

The applicability of this concept is questionable in the case of conventional detectors that are operated to simulate site sizes below 300 nm. Site sizes in the nanometer range using centimeter diameter detectors require reducing the gas pressure and density to very low values. The size of the avalanche region, for nanometer site sizes, may be as large as the sensitive volume of the detector or even larger. In this situation, some of the original ion pairs are formed inside the gas avalanche region. Thus the gas multiplication process depends on the position of the primary ion formation.

Monte Carlo studies have been performed to study the electron avalanche in situations where the Diethorn approximation predicts that uniform multiplication is not possible. Segur *et.al* have derived an expression for gas multiplication factor in small

detectors at low pressure values (15). In such situations, the primary electron produced near the anode will rotate around the anode before being collected at the anode resulting in an avalanche region which is much smaller than predicted by the Diethorn equation.

Wall Effect and Wall-less Counter

A walled counter consists of a gas filled probe, surrounded by a solid wall, the medium. The atomic composition of both the media and the wall is the same resulting in a homogeneous state. Bragg-Gray cavity theory and Fano theorem, a mathematical approach to relate the dose in the probe to the dose in the wall, show that the total energy deposited in the gas filled cavity is the same in the wall material, if, the density effect on stopping power is neglected.

With this assumption, the energy absorbed per unit mass is the same in wall and gas medium. In microdosimetric measurements, the dimensions of the simulated sites are always smaller than the range of the particles. This combined with the density difference in the wall and the gas medium, results in smaller or larger number of events in the gas medium. This is called the Wall Effect. Wall effect is a multifaceted phenomenon, contributing to the distortion in the original number of events, depending upon the type of radiation. The different types of wall effects, namely: re-entry effect, v effect and δ ray effect are distinguished by the order in which the ionizations are produced as well as location at which they are produced. However, the time intervals are far too short to be resolved by real time detectors and the sum of the energy from the components of the

track is measured. The solution to this is to have a wall-less detector, which removes the density change at the boundary.

For α particles, the δ ray type wall effect is the primary concern. In Figure 3, a diagrammatic representation of the δ ray effect is shown.

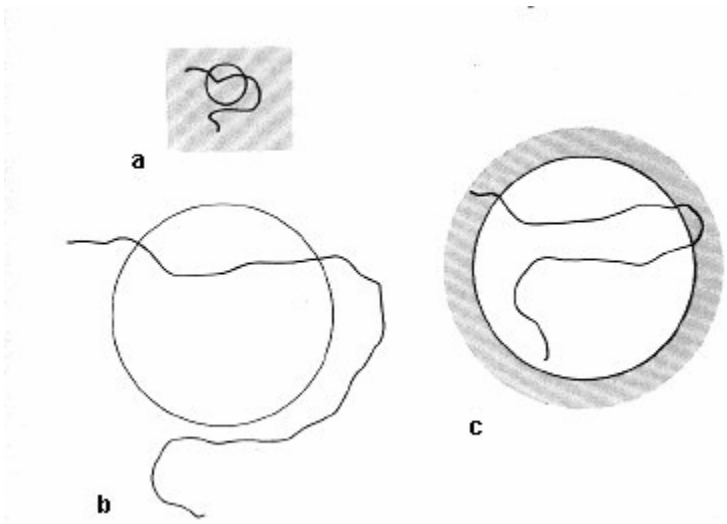

FIGURE 3: Delta Ray Effect.
(a) Represents the entry of a δ ray into a spherical site in a high-density medium. (b) Represents the δ ray effect: The density difference between the cavity and the surrounding material results in the simultaneous entry of the primary particle and the δ ray. (c) Represents the entry of a δ ray in to a spherical site in a low-density medium. The magnification shown represents the difference in the density (3).

As explained in Chapter I and from Figure 3-c, the δ rays, which would have missed the detector volume if the density was the same, appear simultaneously in the gas cavity. In such cases we have no way to distinguish between the α particles and the δ rays. To overcome this problem, wall-less counters are built.

CHAPTER IV

PROCEDURE

Objectives

A cylindrical wall-less proportional counter of diameter 1mm and height 1mm was designed to suit our need to study the microdosimetric spectra of α particles and their δ rays. The objectives in designing the detector were to build a modular detector with mechanical stability and reliability, reduced system noise and minimum usage of insulators.

An iterative method of designing and constructing the detector was followed, which was instrumental in achieving the objectives.

Detector Design

This section describes in detail each and every step involved in the design of the detector, the new techniques that are adopted for detector construction and the advantages of design alternatives and construction techniques relative to others.

For easy understanding, a sketch of the detector components is shown in Figure 4.

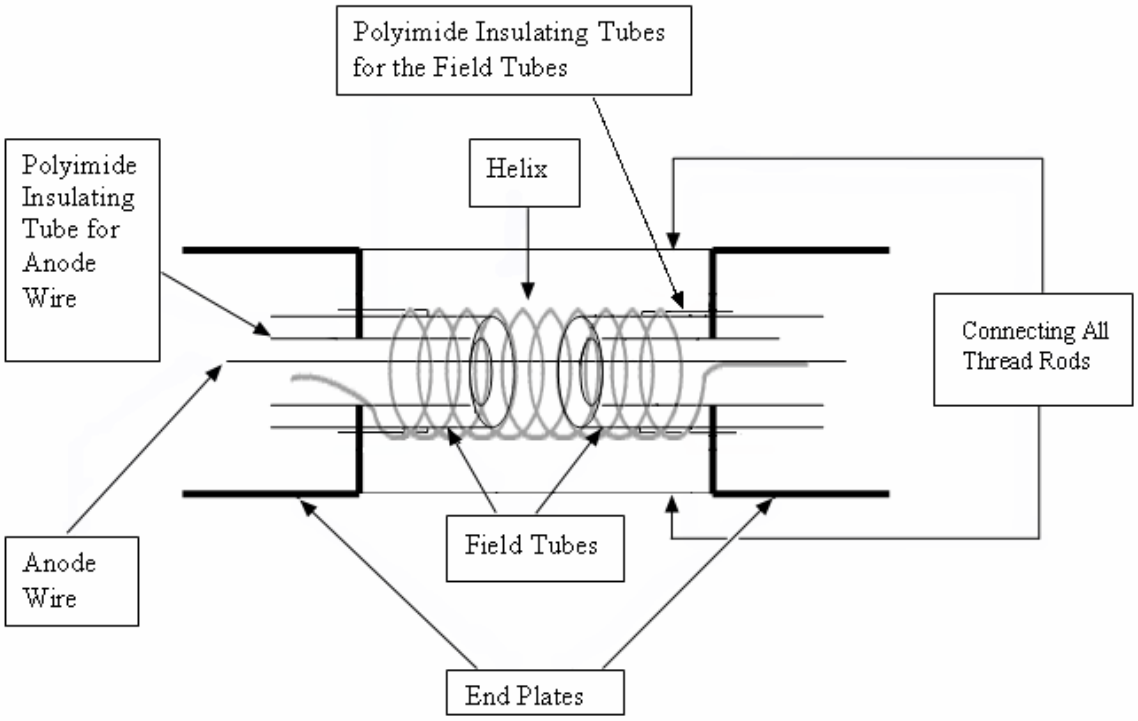

FIGURE 4: Sketch of the Detector Components.
(Sketch not to scale)

Two square plates of size 29.5 by 29.5mm were cut from a pre-perforated circuit board. These end plates are separated by a distance of 25.4mm and held together by four 2-56 connection screws. These end plates serve as a holder for detector components, provide insulation and also act as points for electrical connection to the detector components.

Helix Design

The helix provides a fairly uniform electric field at the anode surface and serves as a cathode, to be held at a negative voltage. The helix for the detector is obtained by

winding a 304 stainless steel hard drawn wire with 0.0508mm diameter, on to stainless steel tube, using a lathe. A hard drawn wire is preferred over a soft drawn wire for its stiffness, tensile strength and limited elasticity. These characteristics allow maintaining the helix shape which is not possible with a soft drawn wire. Also it is preferred to have a helix wire that is not too small in diameter, say, 0.0254mm. As the thickness of the wire becomes smaller, it is more difficult to obtain uniform spacing between the turns of the helix.

The diameter of the helix defines the diameter of the detector. The stainless steel tubing used for winding the helix, has a diameter 25% smaller than the inside diameter of the helix, to take into account the spring back of the wire after winding (11). The maximum spacing between turns of the helix should be no more than half the distance from the helix to the anode to ensure uniform electric field along the length of the anode. Minimum of four turns, with equal spacing between the turns, is necessary. The area of this number of turns accounts for 20% of the surface area of the detector cylinder, leaving the remaining 80% uncovered. Once the required size helix is obtained, it is attached to the end plates forming the cathode structure. A 6mm long piece of polyimide tubing[1] of 0.86mm diameter is used to support each end of the helix and to insulate the field tubes from the helix. The outside diameter of the polyimide tubing should be equal to the inside diameter of the helix, so that the helix will be accurately centered when it is inserted on to the polyimide tube. Then the ends of the helix on both sides are tied to screws on the end plates. Initially the end plates are assembled with the ends of the polyimide tubing touching. To have a helix without any sag, the nuts on the support screws were adjusted

[1] Source: COLE PARMER INSTRUMENT COMPANY

slowly to increase the distance between the end plates and tension the helix. The helix can be adjusted by moving the nuts in or out. By tightening the screws to the right extent, a straight and a firm helix is obtained. The use of hard drawn wire and this method for adjusting helix tension obviates the need to use support wires to prevent the helix from sagging. When the helix is properly adjusted, jam nuts on the outside of the end plates are used to secure the structure. The screws used for securing the helix, also serve as connection points to supply negative voltage to the helix. This method of using screws to secure the helix helps in removing the helix, without any damage, at any time.

Field Tubes

Once the arrangement had been made for the helix placement, the field tubes were inserted into the polyimide tubing which supports the helix. The diameter of the polyimide tubing was chosen in such a way that its outer diameter would enable the helix to slide on and the inner diameter would be large enough to insert the field tube. The field tubes were made from 0.51mm diameter stainless steel tubing. The field tubes were inserted to a point where they would be held 1mm apart once assembled. This distance defines the height of the detector volume. The length of the field tubes was chosen so that they would protrude a sufficient distance from the outer surface of the end plates to facilitate electrical connection. The field tubes are held in position by securing it to the end plates using a dab of epoxy. The field tubes are held at an intermediate potential relative to the cathode and the anode. The intermediate potential that has to be applied to the field tubes is (16):

$$V_f = V_h \bullet \frac{[\ln(r/a)]}{[\ln(b/a)]} \tag{25}$$

where V_f is the voltage to be applied to the field tubes;

V_h is the voltage applied to the helix;

a is the anode radius;

b is the radius of the helix;

r is the radius of the field tubes.

Substituting the specifications used in this experiment:

a = 0.0254mm, b = 1mm and r = 0.51mm,

$$V_f = 0.81V_h \tag{26}$$

A potential divider circuit was put in place to supply the voltage to the field tubes. The details of the potential divider circuit are shown in Figure 5. It represents the exact replica of the circuit, in terms of the number of resistors and capacitance used.

Anode Design

Polyimide tubing of diameter 0.086mm, which would act as an insulator for the anode, was inserted into the field tube. Then the anode wire was passed through the polyimide tubing and secured at both the ends. Again, the polyimide tubing diameter was chosen in such a way that it can be inserted into the field tube and also will allow insertion of the anode wire. Commercial availability of the required size polyimide tubing has obviated the need for a hand made glass insulator.

The anode wire used in this experiment is an annealed 304 stainless steel wire with a diameter of 0.0254mm. The anode wire must be under tension after installation to keep it

straight. For this small diameter of the anode wire, a cantilever spring is used to provide tension.

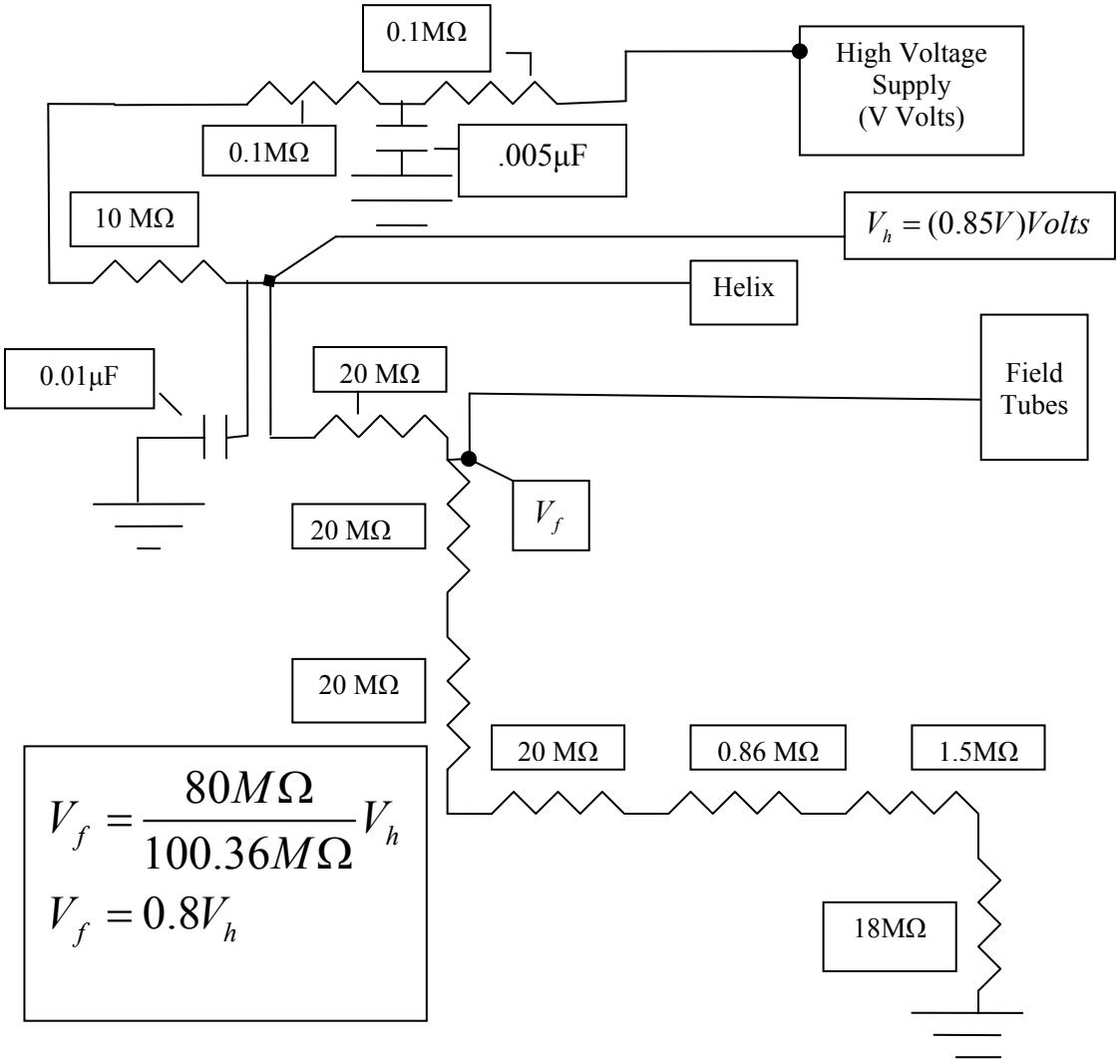

FIGURE 5: Voltage Divider Circuit for the Field Tubes.

A cantilever spring is obtained by taking a piece of a piano wire, of 0.35mm diameter, and forming an eye on one end. This end is anchored to the end plate by a screw. The

other end of the cantilever is formed into a shallow ‘v’ to place the anode wire. The anode wire is looped around the cantilever and is tensioned by hanging a small weight on its free end. The ‘v’ area of the cantilever was tinned before passing the anode wire and a home made flux was used with a needle tip solder iron to clamp the wire. The home-made flux was prepared by mixing 29% of ammonium chloride and 71% of zinc Chloride in water (17).

The other end of the anode wire does not require a spring and is anchored to a copper bar placed on the end plate. This serves as a point for electrical connection to the anode wire. The anode is maintained at ground potential and connected to the pre-amplifier. A photograph of the detector assembly is shown in Figure 6.

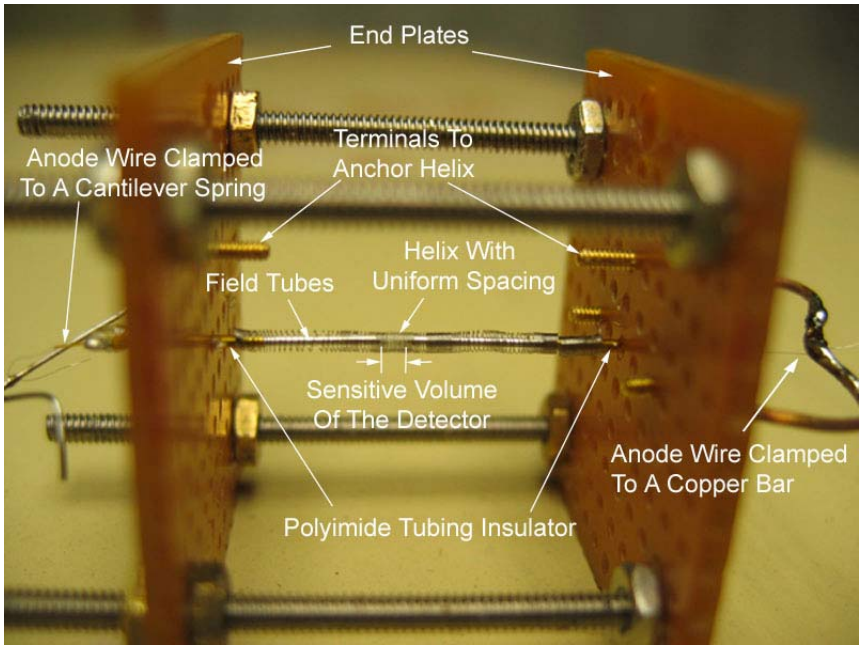

FIGURE 6: Photograph of the Detector.

Detector Setup Description

The detector, along with a charge sensitive pre-amplifier, is housed inside a vacuum chamber. Vacuum condition inside the chamber is obtained by using a Trivac Vacuum pump. The vacuum chamber set up consists of a Pyrex glass bell jar with aluminum coating on the inside that fits into a circular aluminum base. An O-ring between the aluminum base and the bell jar provides an air-tight seal. A 43.1cm tall Pyrex jar is used so that there is no space constraint inside the chamber. The vacuum chamber material has been carefully chosen weighing all the factors that would favor gas purity leading to undistorted gas gain (12). The aluminum base sits on top of a three-legged stand attached to it. All the feed-throughs to the detector are provided through the aluminum base. Vacuum seal is maintained for all the feed-throughs in the aluminum base. To shield the chamber electrostatically, a copper cylinder of height 47cm and diameter 27cm is used to cover the bell jar. This arrangement helps to minimize electromagnetic interference.

Copper tubes equipped with a brass bellows sealed valve provide the gas connection to the detector system. Quarter inch Swagelok ® compression fittings and ferrules are used for sealing the copper tubes. To conveniently monitor the pressure inside the chamber, two pressure gauges, one in the range of 0 to 50 torr and the other in the range of 0 to 800 torr, are connected. Once vacuum of about 0.6 torr is obtained, by pumping, propane gas is leaked into the system to the required pressure. A picture of the detector vacuum setup and gas flow system is shown in Figure 7.

A 1 microcurie sealed Am-241source is placed inside the chamber, attached to a rotatable, sliding vacuum feedthrough. This enables the source position to be changed relative to the detector without the need for opening the chamber.

FIGURE 7: Snapshot of the Detector System with the Vacuum Setup and Gas Flow Connections.

A Canberra Shaping Amplifier Model 2011 was connected in series to the output of the preamplifier. The preamplifier and the amplifier were powered by a Tennelec NIM (Nuclear Instrument Module) bin supply. Bias to the detector was applied from a Canberra 3002D High Voltage supply. Both the Accuspec MCA and a Tektronix

Oscilloscope were connected to the amplifier output. A Tennelec 202 BLR Pulser was used to supply a test input pulse as part of the quality assurance test for the detector and the pre-amplifier. A block diagram of the detector setup is shown in Figure 8.

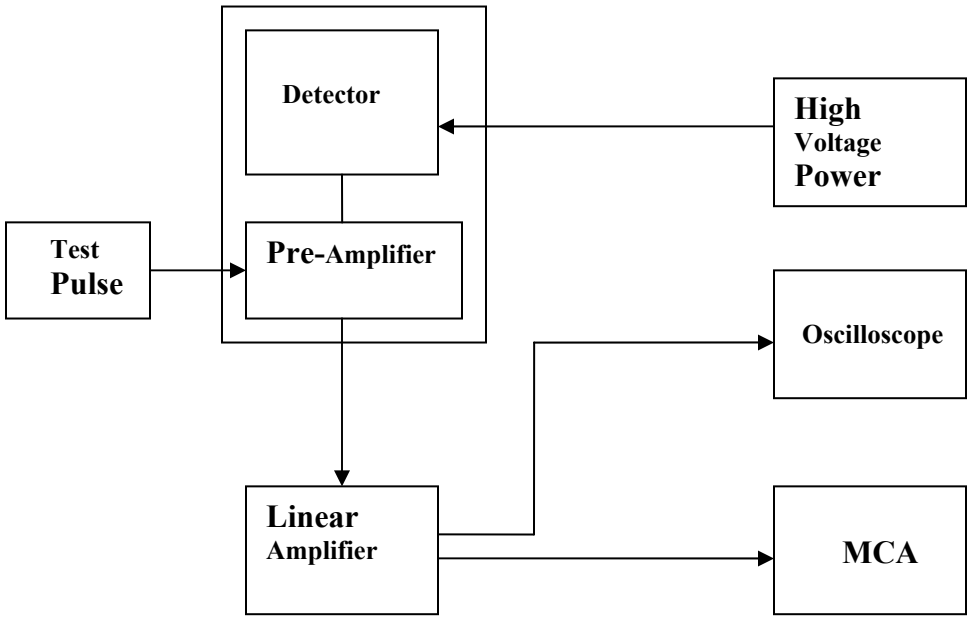

FIGURE 8: Block Diagram of the Detector Setup.

The detector is held on to the fork arms of an aluminum frame inside the vacuum chamber. Figure 9 shows a picture of the detector arrangement inside the vacuum chamber.

Once the detector position was fixed in the vacuum chamber, electrical connections were made to the helix, the anode, and the field tubes. Because of the high resistances involved, a conventional ohm meter could not be used to test the circuit. Instead voltages to the helix and the field tubes were measured using an electrostatic voltmeter. Output at the oscilloscope was measured for a test input from the pulser to ensure the operation of the pre-amplifier.

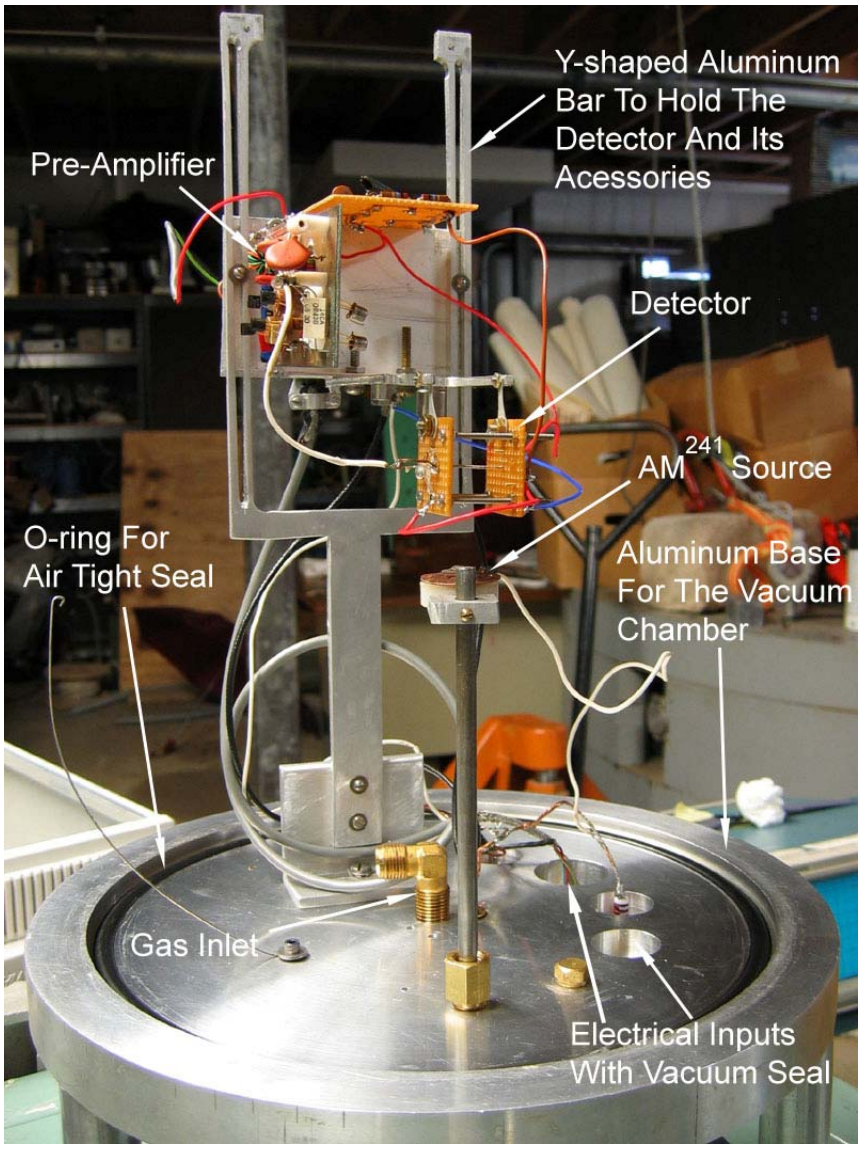

FIGURE 9: Arrangement of Detector and its Components Inside the Vacuum Chamber.

The linearity of the amplifier was tested with a series of pulses with a constant step increase in the amplitude. The output at the MCA reflected the changes in the amplitude. Once the electronics were verified, the chamber was closed and was evacuated to about 0.6 torr**.** Then the chamber was filled with propane to the required pressure.

CHAPTER V

RESULTS

Operating Voltage

The first step of the data acquisition procedure is to determine the operating voltage of the detector, where the true proportionality mode is maintained. Output pulses were observed for voltage increments of 50 volts, starting from 100 volts. Once the voltage that produced detectable gas gain was reached, voltage was increased in steps of 25 volts until indications of potential breakdown (long or irregular preamplifier output pulses) were detected. The operating voltage just below the breakdown potential, 425 volts was selected for the rest of the work. Gas gain, at 425 volts, as a function of pressure was determined from measurement of the pulse height produced by the α particle crossing the site and the charge per channel calibration obtained from the MCA calibration data. Figure 10 shows the variation of a gas gain as a function of pressure.

Noise Level

Next, the noise level in the detector assembly was determined in terms of channel numbers of the MCA. This was obtained by covering the source, inside the vacuum chamber, with aluminum foil. The thickness of aluminum foil was chosen so that no α

particle would be able to reach the detector. Also the source was kept at the farthest position from the detector. In this condition, the counts at the MCA are a measure of the

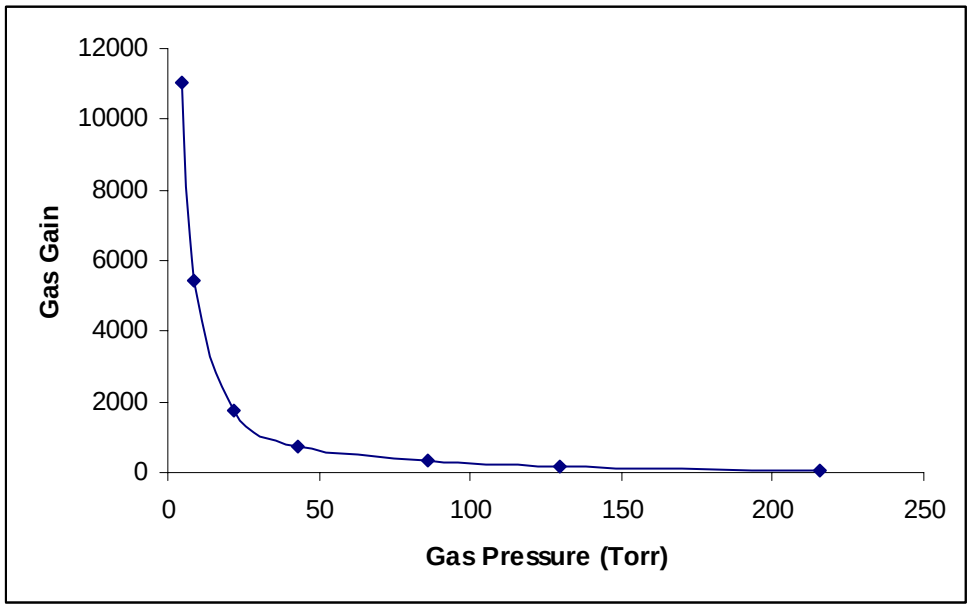

FIGURE 10: Variation of Gas Gain as a Function of Gas Pressure.

noise in the system. The peak channel number from this measurement is set as the lower level discriminator (LLD). For this experimental setup the noise level in terms of channel number was found to be **60**.

Baseline Offset

The inherent shift in the channel numbers of the MCA due to the Analog to Digital Converter (ADC), is determined by testing the ADC with a series of pulses, with constant increase in amplitude. This procedure will determine the accurate baseline offset of the ADC, for a given amplification chain.

The baseline offset for the ADC in the MCA system was found to be **49 channels.** This result was obtained from a plot of channel number *vs.* pulse amplitude, for a constant increase of 0.025 millivolts, shown in Figure 11.

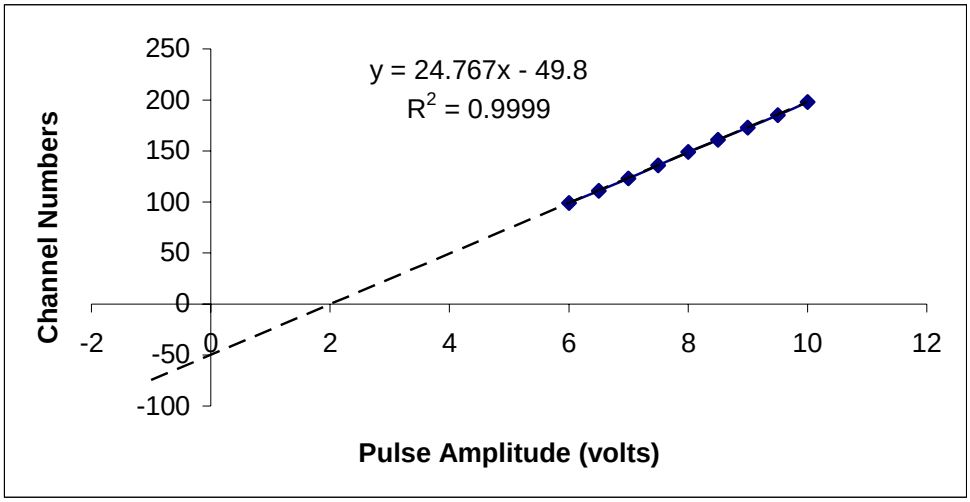

FIGURE 11: Baseline offset for the Detector System.
Baseline offset for an increase of 0.025 millivolts in pulse amplitude, at a linear amplifier gain of 1k.

Functionality Check for the Detector

To determine the functionality of the detector in micro and nanometer dimensions, lineal energy spectra for α particles from Am-241, were obtained for site sizes ranging from 500 nanometer to 10 nanometers. The pressure of the gas required to simulate different site sizes are tabulated in Table 1.

Once the spectra have been collected for different site sizes, calibration of the spectra has to be performed. The calibration of the spectra converts channel number to lineal energy, *y*.

Calibration Procedure

Since the most probable chord length for random tracks through a cylinder with its height equal to its diameter, is the diameter, the channel with the peak count rate in the MCA data corresponds to the energy deposition produced by the product of the LET of the α particles and the simulated site size.

Am-241 primarily emits monoenergetic α particles of energy 5.57 MeV with yield of 85.27%. Am-241 also emits α's with energies 5.46 and 5.33 MeV with very low yields of 1.59% and 12.57% percent respectively. The LET of 5.57 MeV α particles from Am-241 in propane, is 90 keV/μm. The product of stopping power and diameter, which gives the energy deposition, when divided by the mean chord length gives the lineal energy at that channel number. [Equation (5) gives the mean chord length of a cylinder with equal height and diameter]. Accordingly, all the channel numbers are expressed in terms of lineal energy.

Pulse height spectra for site sizes 500nm, 300nm, 200nm, 100nm, 50nm, 20nm and 10nm were obtained, to establish the functionality of the detector. From the pulse height spectra, the peak channel number for different simulated site sizes was obtained.

Figure 12 shows the pulse height spectrum for a 100nm site size diameter. This figure serves as a sample of the pulse height spectrum. For all the site sizes the shape of the pulse height spectrum follows the expected bell shaped curve with a tail end on the right side, due to straggling effects. The left side of the spectrum in the first few channels represents the contribution from electronic noise and energy deposition from δ rays.

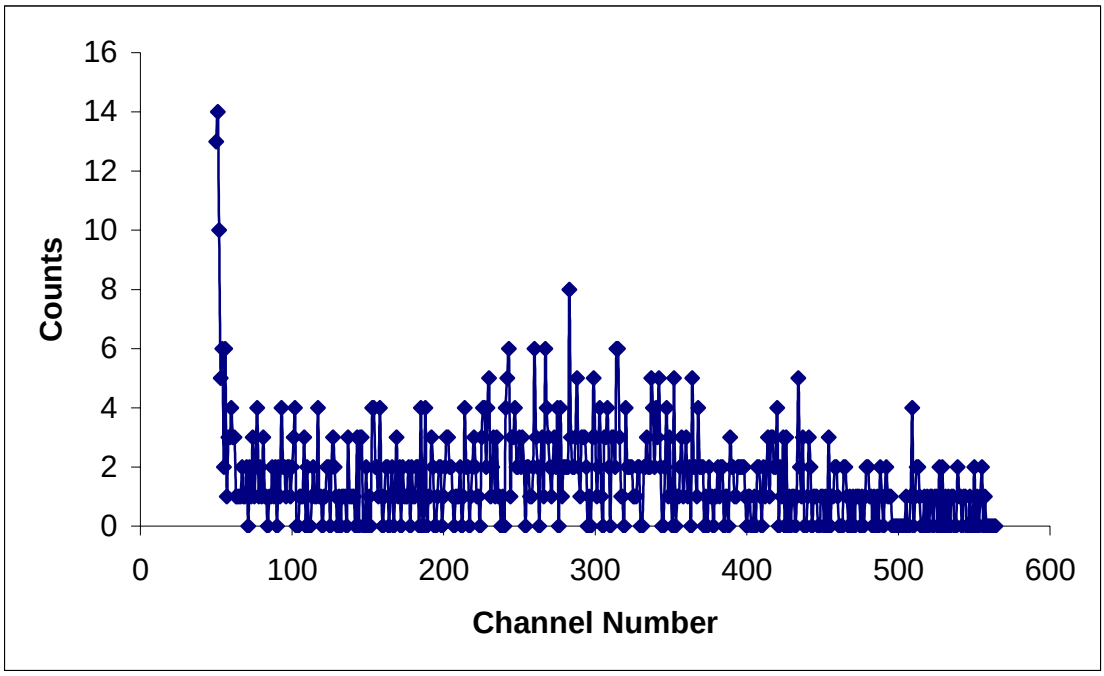

FIGURE 12: Pulse Height Amplitude Spectrum from the MCA for a 100nm Site Size Diameter.

Figure 13 shows the variation in the peak channel number as a function of gas pressure and also as a function of site sizes.

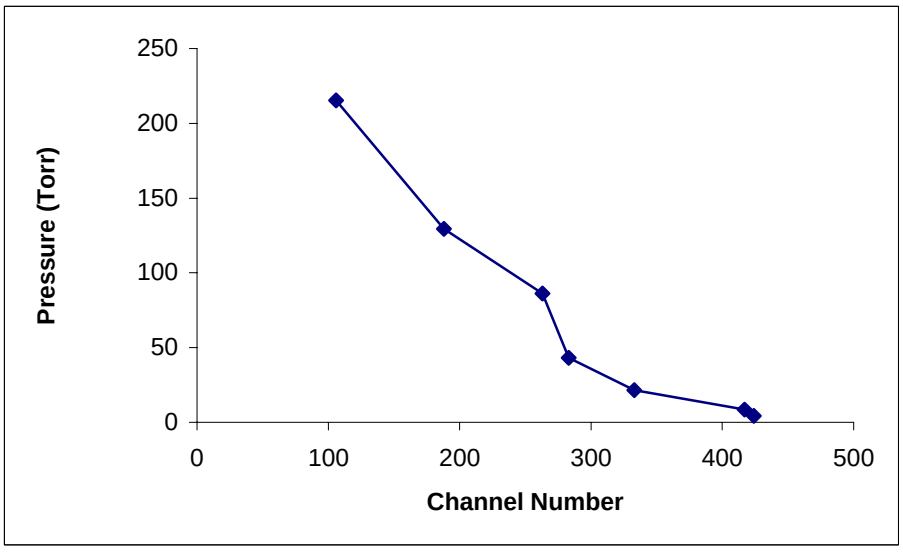

FIGURE 13: Peak Channel Number as a Function of Gas Pressure and Site Size.

Calibration was performed at these peak channel numbers and the lineal energy per channel number was calculated for all the simulated site sizes. Table 2 represents the lineal energy per channel number for the different site sizes.

TABLE 2: Lineal Energy Calibration for Simulated Site Sizes.

Simulated Site Size (nm)	Lineal Energy/Channel (y/keV)
500	1.27
300	0.72
200	0.51
100	0.48
50	0.40
20	0.32
10	0.32

Data Analysis

After calibration of the acquired spectrum, the data can be shown in the form of number of counts *vs.* lineal energy. However, since values of lineal energy spectra span over a very large magnitude, a preferred format for representing the lineal energy spectra is a semi-log representation of:

(1) $y * f(y) vs \log y$, where $f(y)$ is the fraction of events between y and $y + dy$, and

(2) $y * f(y) vs \log y$, where $d(y)$ is the fraction of dose delivered by events between y and $y + dy$

To express this data in the preferred format of lineal energy, each channel with the corresponding counts and lineal energy are grouped into bins. The numbers of channels in each bin is increased, every five bins, by a factor of 2^n, where n starts from zero and continues until all the channels in the spectrum are covered. The fraction of events and the average energy in each bin are calculated. From this $y * f(y)$ and $y * d(y)$ for different simulated site sizes are calculated. A correction factor for the DAC offset has been included in this calculation.

The $y * f(y) vs \log y$ and $y * d(y) vs \log y$ for different simulated site sizes are represented in the Figures 14 through 27.

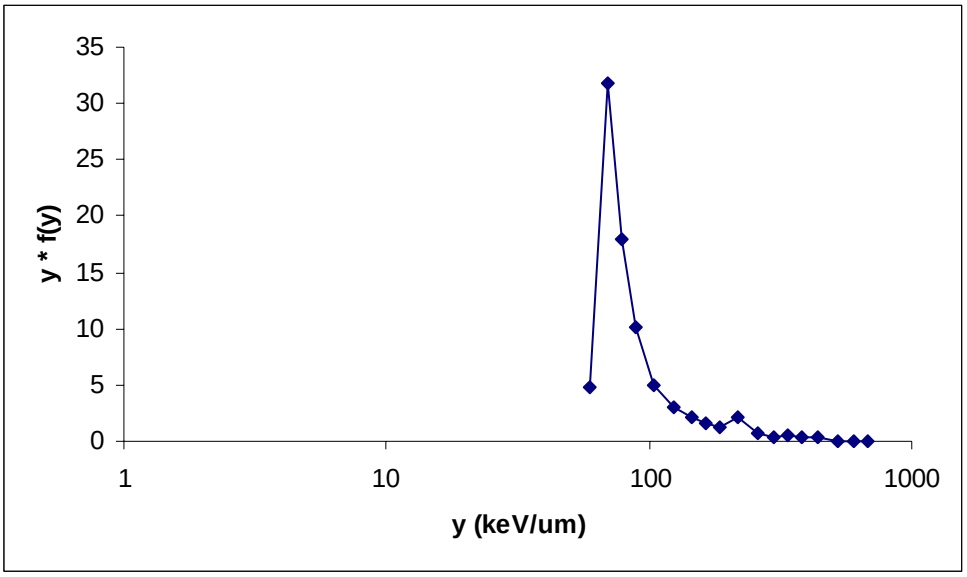

FIGURE 14: Frequency Distribution of Events Due to α Particles of Energy 5.57 MeV in a 500 nm Site Size Diameter.

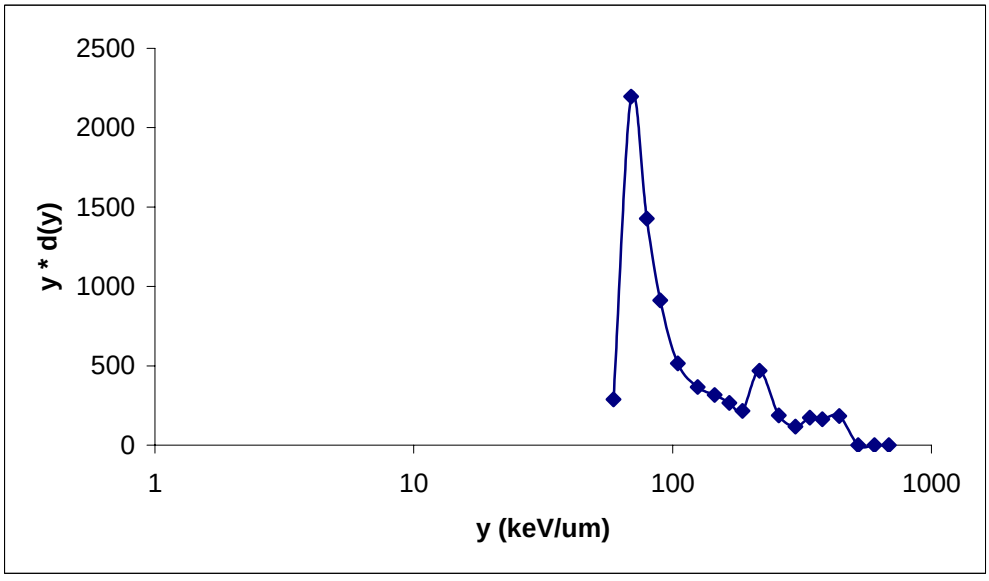

FIGURE 15: Dose Distribution Due to α Particles of Energy 5.57 MeV in a 500 nm Site Size Diameter.

In the frequency distribution spectra, the area under the curve delimited by any two values of y is proportional to the fraction of events in that range of lineal energy. Similarly the area under the dose distribution spectra delimited by any two values of y is proportional to the fraction of dose delivered by events with lineal energies in that range.

From Figures 14 and 15, the lineal energy spectra for 500nm site size, show contributions from electronic noise, the peak at around 90 kev/μm, along with the energy deposition due to α particles. At site size of 500nm, the major contribution to the dose should be from α particles. Since that is not seen in Figure 14, it can be concluded that the reliability of the detector at higher site sizes is questionable. This behavior is not unexpected, considering the small dimension of the detector, 1mm that requires a gas pressure of 215 torr to simulate 500nm site size diameter.

Lineal energy spectra for all other site sizes, from 300nm to 10nm, follow the expected shape and this establishes the functionality of the detector at smaller site sizes. Lineal energy spectra for the simulated site sizes are represented in Figures 16 through 27.

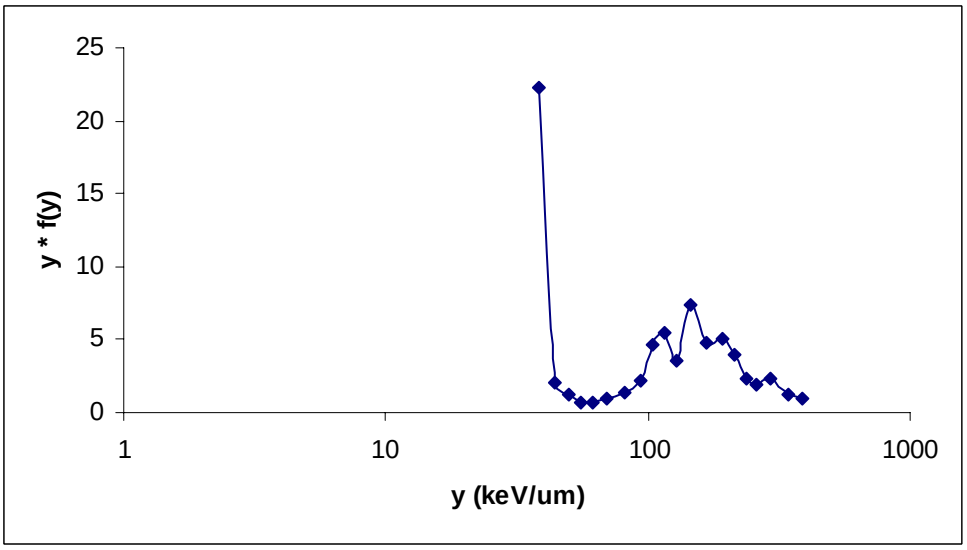

FIGURE 16: Frequency Distribution of Events Due to α Particles of Energy 5.57 MeV in a 300 nm Site Size Diameter.

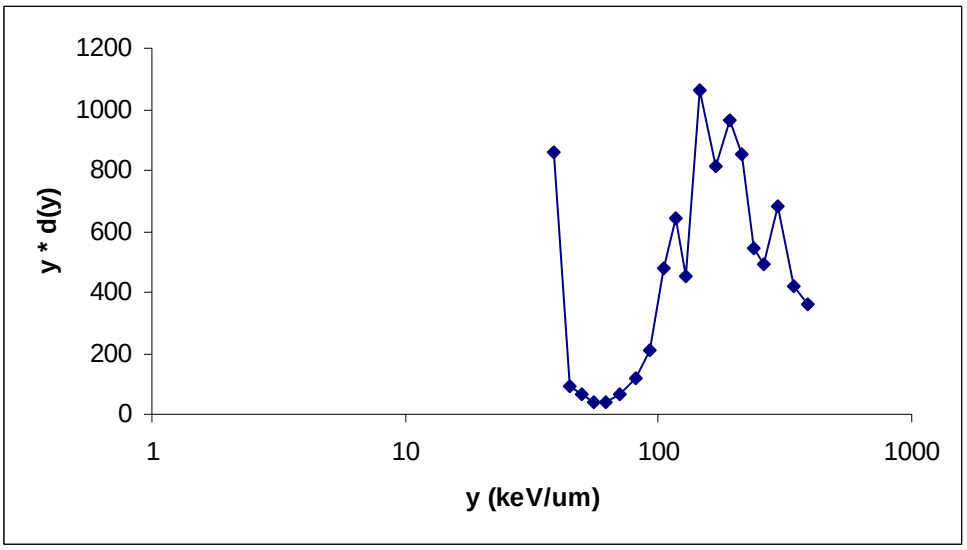

FIGURE 17: Dose Distribution Due to α Particles of Energy 5.57 MeV in a 300 nm Site Size Diameter.

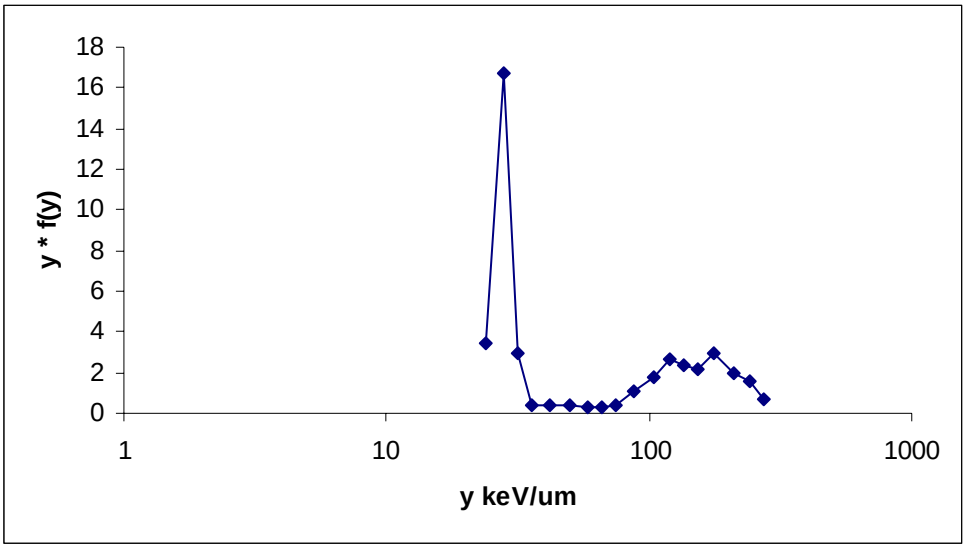

FIGURE 18: Frequency Distribution of Events Due to α Particles of Energy 5.57 MeV in a 200 nm Site Size Diameter.

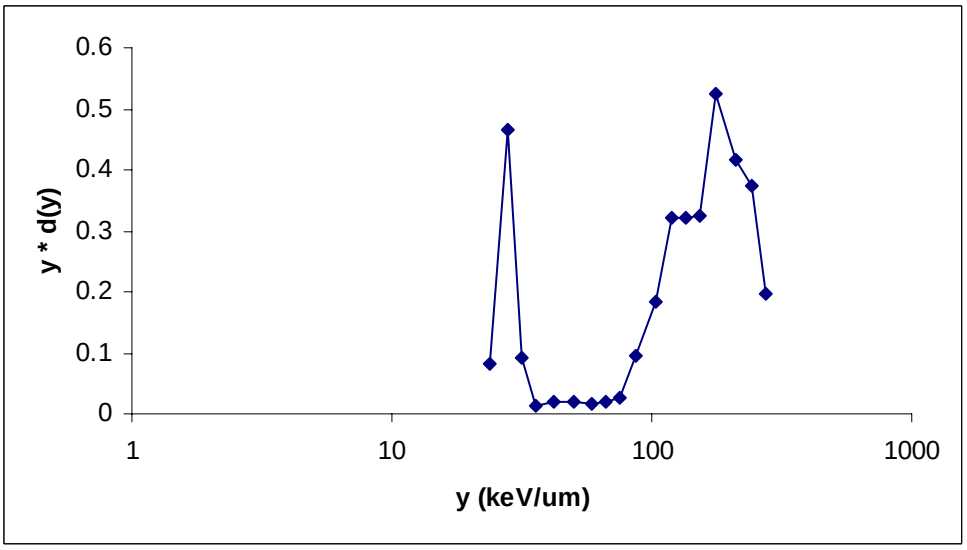

FIGURE 19: Dose Distribution Due to α Particles of Energy 5.57 MeV in a 200 nm Site Size Diameter.

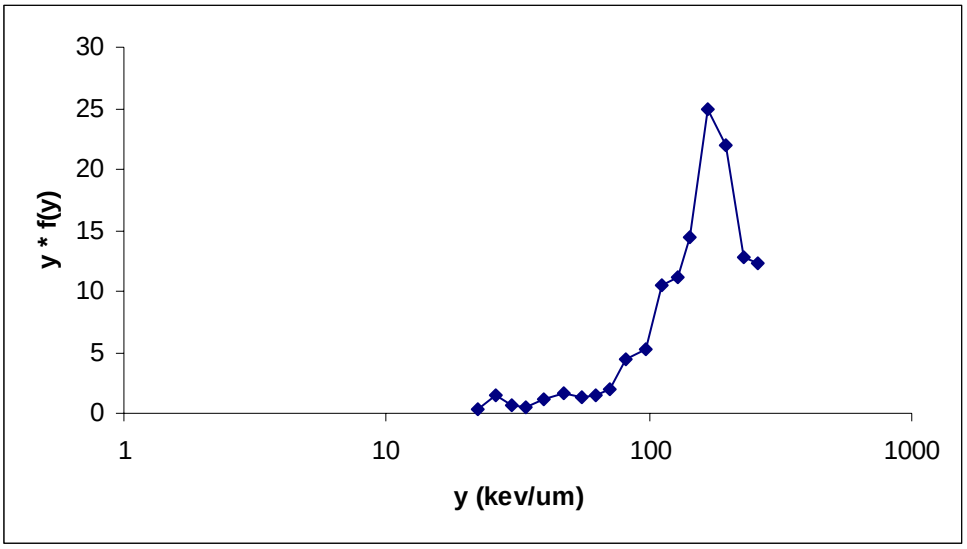

FIGURE 20: Frequency Distribution of Events Due to α Particles of Energy 5.57 MeV in a 100 nm Site Size Diameter.

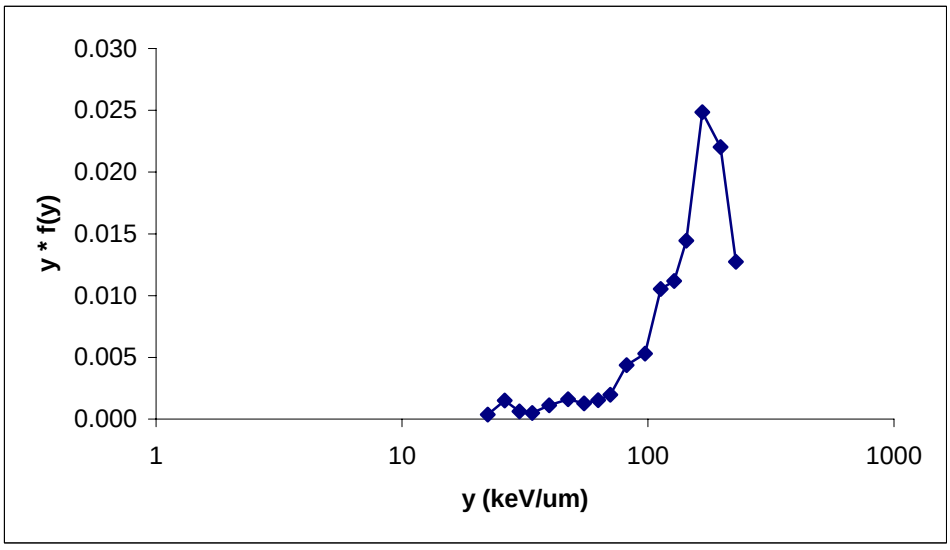

FIGURE 21: Dose Distribution Due to α Particles of Energy 5.57 MeV in a 100 nm Site Size Diameter.

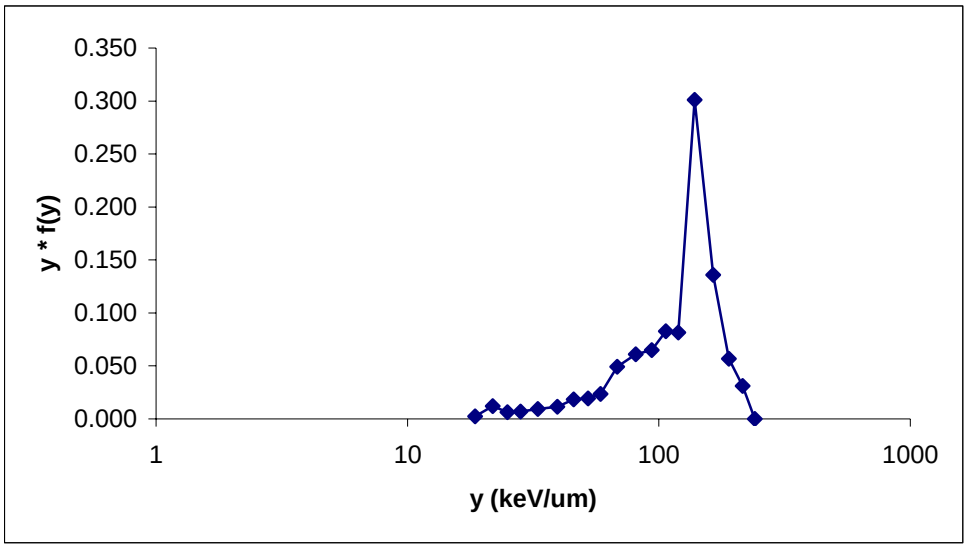

FIGURE 22: Frequency Distribution of Events Due to α Particles of Energy 5.57 MeV in a 50 nm Site Size Diameter.

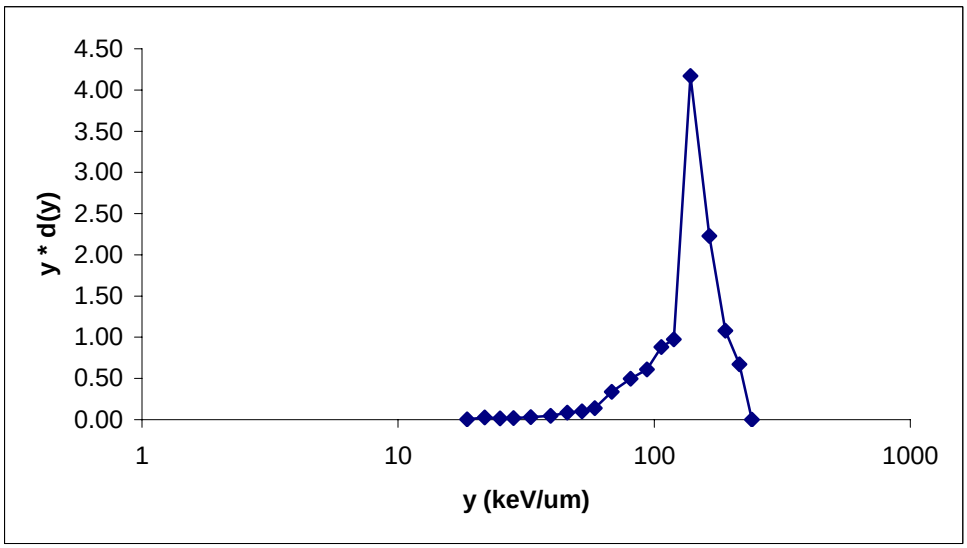

FIGURE 23: Dose Distribution Due to α Particles of Energy 5.57 MeV in a 50 nm Site Size Diameter.

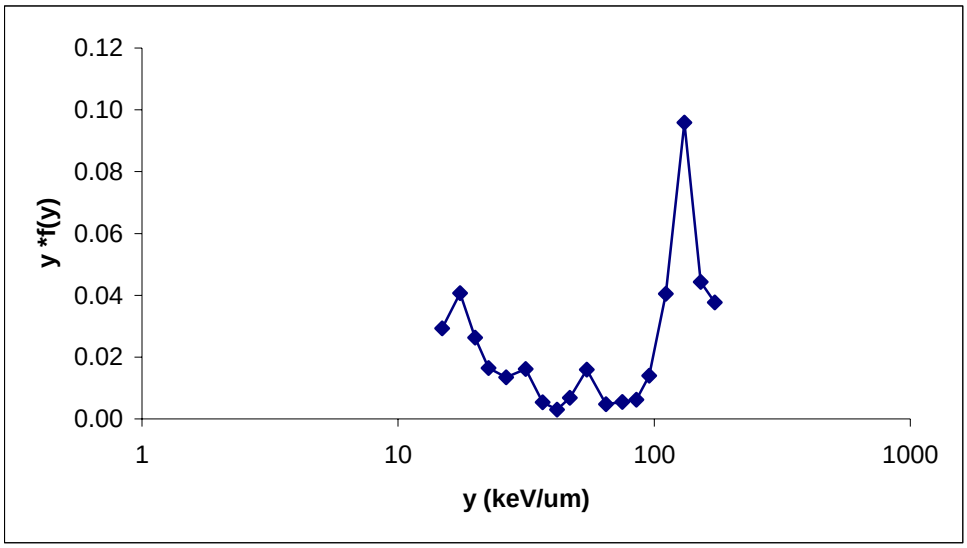

FIGURE 24: Frequency Distribution of Events Due to α Particles of Energy 5.57 MeV in a 20 nm Site Size Diameter.

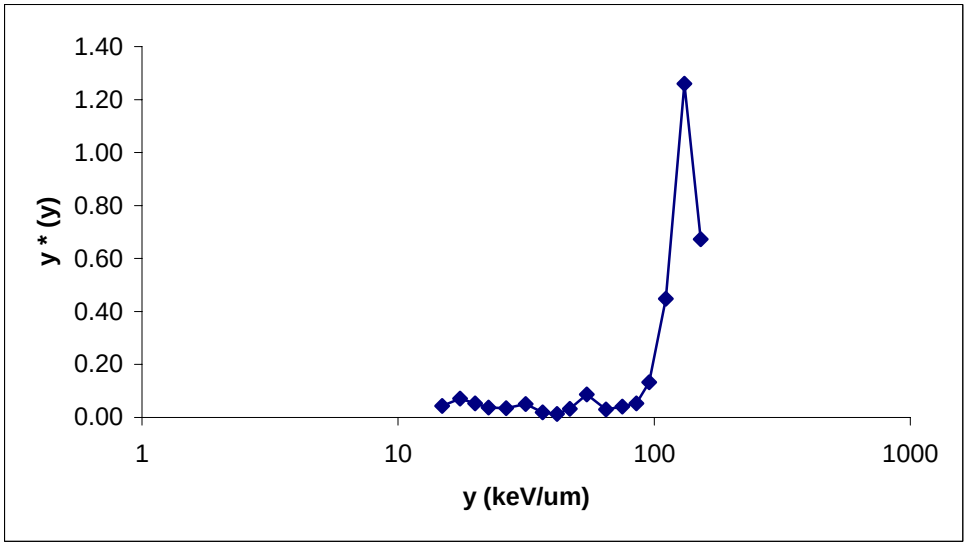

FIGURE 25: Dose Distribution Due to α Particles of Energy 5.57 MeV in a 20 nm Site Size Diameter.

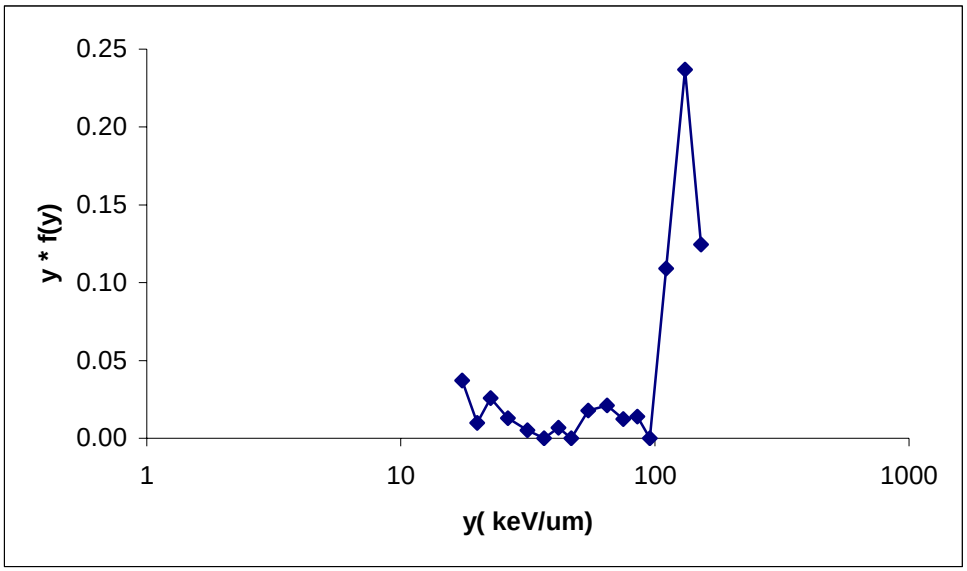

FIGURE 26: Frequency Distribution of Events Due to α Particles of Energy 5.57 MeV in a 10 nm Site Size Diameter.

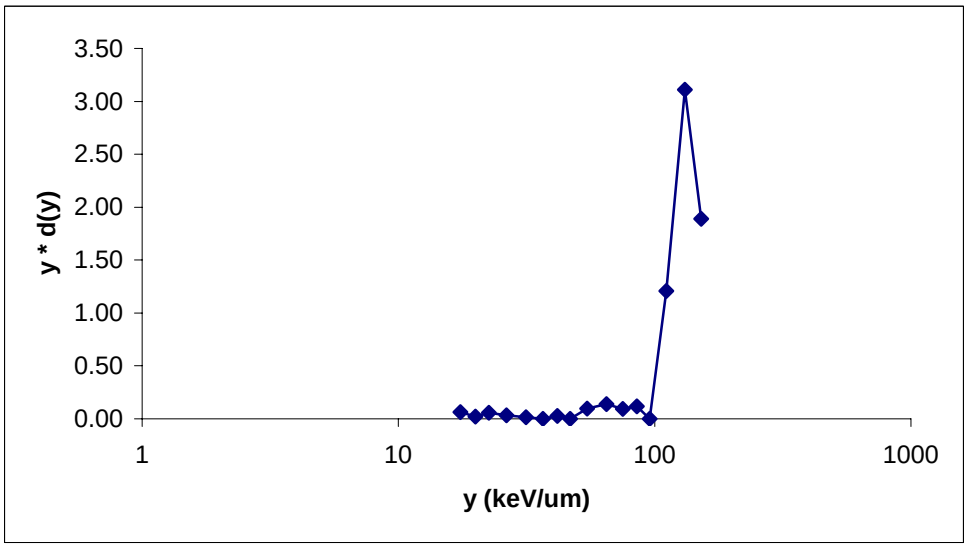

FIGURE 27: Dose Distribution Due to α Particles of Energy 5.57 MeV in a 10 nm Site Size Diameter.

As the site size decreases, the contribution due to δ rays also increases. Since the detector gain increased, the largest events in the 20 and 10nm sites exceeded the MCA and a lower amplifier gain setting would have made the energy loss straggling more visible.

CHAPTER VI

SUMMARY AND CONCLUSIONS

As explained in the introduction, knowledge about energy deposition due to radiation at the cellular level – at nanometer dimensions – is essential to understand the biological effects of radiation. This work has resulted in the development of a practical tool to study such energy deposition experimentally at nanometer dimensions.

The core contribution of this work is the careful choice of novel design techniques resulting in a practical and functional detector for energy deposition at nanometer dimensions. The design has been refined by evaluating alternative procedures and adopting methods that lead to a modular small size detector. The cylindrical wall-less proportional detector, thus constructed, was tested with 5.57 MeV α particles using an Am-241 source. The spectra obtained from the experimental study were analyzed to assess the detectors reliability.

Functionality tests executed on the detector have proven that the detector operates reliably at dimensions as small as 10nm. The results obtained from this study shows that the detector operates better at nanometer dimensions than at micrometer dimensions. A possible explanation for this phenomenon might be the very small dimension of the detector, 1mm, which in turn requires a high gas pressure of 215 torr to operate at 500nm. This observation concurs with studies on the influence of the size of the detector on site size simulation (3). Also, a better microdosimetric spectrum at 500nm site sizes could

have been obtained in this study if the voltages were adjusted to obtain approximately a constant gas gain.

Availability of a functional detector at nanometer dimensions opens up the potential for building a bridge to relate the microdosimetric spectra to the radiobiological effects of α particles and their δ rays. Future research studies could be designed to use the detector for such applications.

There is also scope for further refinement of the detector design. In the current detector, the gas purity in the detector system has been well maintained, with a leak rate of 0.8torr in 24 hours. If the detector has to be operated at site sizes as small as 5nm, which requires a gas pressure of 2 torr, a leak rate of 0.8 torr would affect the gas gain. Improvements to the vacuum system would be required for smaller site sizes. A possibility that could be explored is the reduction of external connections from the detector to the gas flow system and the pressure gauges.

As stated at the outset, this work is just a first step, but a crucial step, in furthering our understanding the biological effects of radiation at the microdosimetric levels. With the construction of a functional detector, the prime objective of this project has been achieved. It is our belief and expectation that this detector would be of great value in future studies that would advance our understanding of the biological effects of radiation.

REFERENCES

1. D. T. Goodhead, Track structure considerations in low dose and low dose rate effects of ionizing radiation. *Advance in Radiation Biology*, **16**, 7-43 (1992).

2. A. M. Kellerer, Microdosimetry: Reflections on Harold Rossi. *Radiat. Prot. Dos.* **99**, 17-22 (2002).

3. H. H. Rossi, M. Zaider, *Microdosimetry and Its Applications.* Springer-Verlag, New York, 1996.

4. L. A. Braby, N. F. Metting, W. E. Wilson, and L. H. Toburen, Microdosimetric measurements of heavy ion tracks. *Adv. Space Research*, **12**, **(**2)23-(2)32 (1992)**.**

5. A. H. W. Nias, *An Introduction to Radiobiology*, Second Edition, John Wiley and Sons, New York, 1998.

6. A. J. Waker, Principles of experimental microdosimetry. *Radiat. Prot. Dos.* **61**, 297-308 (1995)**.**

7. A. M. Kellerer, *Analysis of Patterns of Energy Deposition.* EURATOM Report EUR 4452 d-e-f, Brussels. H.G.Ebert edition, 107-134 1970.

8. G. F. Knoll, *Radiation Detection and Measurement*, Second edition, John Wiley and Sons, New York, 1989.

9. P. Kliauga, Design of tissue-equivalent proportional counters. *Radiat. Prot. Dos.* **61**, 309-322 (1995).

10. P. J. Kliauga, Measurement of single event energy deposition spectra at 5μm to 250nm simulated site sizes. *Radiat. Prot. Dos.* **31**, 19-123 (1990).

11. L. A. Braby, G. W. Johnson, J. Barthe, Practical considerations in TEPC design and construction. *Radiat. Prot. Dos.* **61**, 351-369 (1995).

12. ICRU, *Stopping Powers and Ranges for Protons and Alpha Particles.* Report 49, International Commission of Radiation Units and Measurements, Bethesda, MD, 1993.

13. D. R. Lide, *Handbook of Chemistry and Physics*, Student Edition, CRC Press, Boca Raton, FL, 1995.

14. S. B. Guetersloh, *Microdosimetric characterization of energy-deposition patterns near the end of alpha tracks*, M.S Thesis, Texas A&M University, 2000.

15. P. Segur, P. Olko, P. Colautti, Numerical modeling of tissue-equivalent proportional counters. *Radiat. Prot. Dosim.* **61**, 323-350 (1995).

16. A. J. Waker, D. G. Maynard, The effect of geometrical scaling on the gas gain of proportional counters intended for microdosimetric measurements. *Radiat. Prot. Dosim.* **1/2**, 37-40 (1989).

17. R. G. Marcley, Small Mass Spectrometer, Apparatus Drawings Project. Report Number 5, *American Journal of Physics*, **28**, 380-383 (1960).

VITA

Sripriya Rayadurgam has a Bachelor's and a Master's degree in Physics from Madras Christian College, University of Madras, India. While at graduate school, she has been a graduate research assistant for Dr. Leslie A. Braby, Nuclear Engineering Department, Texas A&M University and a Health Physics Trainee at the Nuclear Science Center, Texas Engineering Experiment Station. She can be reached at Nuclear Engineering Dept, Texas A&M University, 3133 TAMU, College Station, TX 77843-3133.